Supplement of The Cryosphere, 20, 4927–4955, 2026
https://doi.org/10.5194/tc-20-4927-2026-supplement

The Cryosphere
Open Access

Supplement of

Annual changes in firn density and compaction under Alpine Climate conditions: first multi-year CMP radar observations from the Grosser Aletschgletscher

Akash M. Patil et al.

Correspondence to: Akash M. Patil (akash.patil@badw.de, akash.patil@fau.de)

S1 Specific notes related to the CMP method section

S1.1 Common midpoint method

The common midpoint method is a geophysical technique primarily used to estimate changes in radar wave velocity with depth in the subsurface by varying antenna spacing with distance and measuring the two-way travel time (Annan and Davis 2003), as shown in Fig S1a. The CMP data gathered during the 2024 and 2025 campaigns use the antenna settings given in Table 2, main text. The measurement technique involves manually triggering the radar pulses at an initial offset of 0.2 m between T_1 *and* R_1. With a constant offset of 0.2 m, by moving T_1 *and* R_1 by 0.1 m on either side of the midpoint (M in Fig S1a), we gathered each trace at each position of T_1 *and* R_1, covering a total offset of 20 m. For example, in our case (Fig. S1a), $D_1 = 0.2\,m,\ D_2 = 0.4\,m$ and $D_3 = 0.6\,m$ we went on till 20 m, with each T_1 *and* R_1 moved by 0.1 m on either side of the midpoint (M in Fig. S1a). An exemplified CMP-generated radargram is shown in Figure S1b after the basic processing steps.

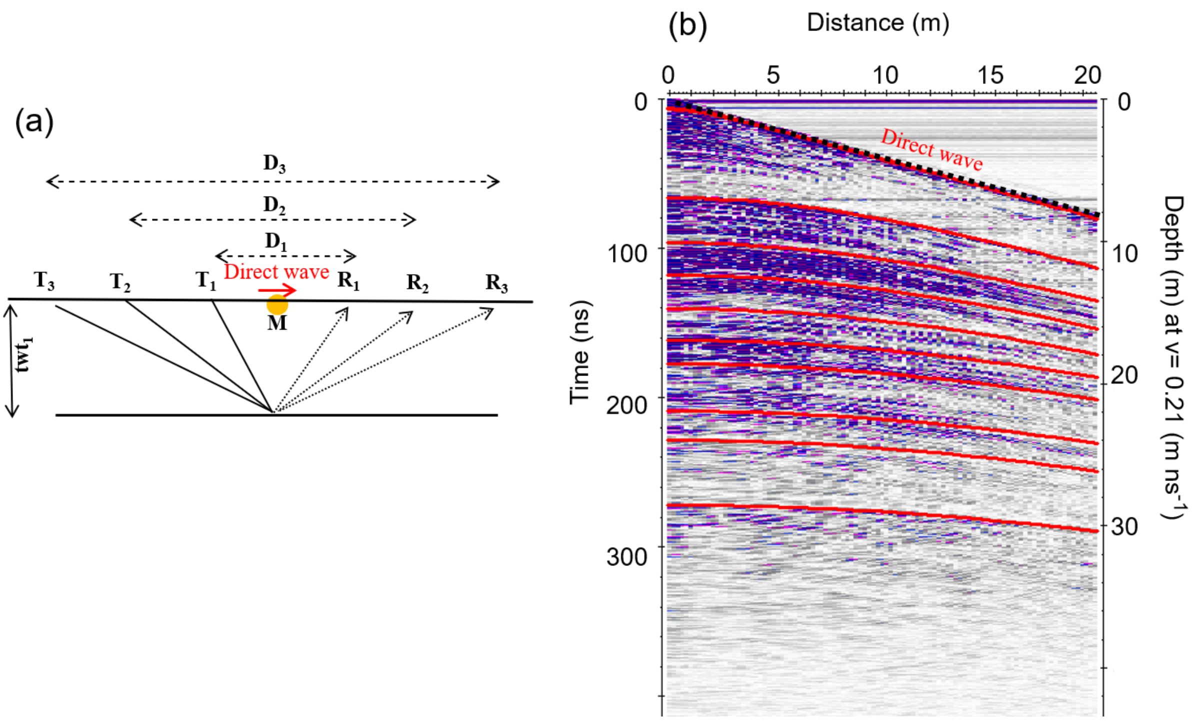

Figure S1: Schematic representation of the common midpoint (CMP) method measurement technique (left) shown for a single reflector, modified after Annan and Davis (2003). T_1 *and* R_1 *represent the positions of the radar transmitter and receiver, respectively, whereas an orange dot depicted as M is a midpoint.* D_1, D_2 *and* D_3 *indicate the offset between* T_1 *and* R_1 *at each location. The direct wave (red arrow) is the radar wave above the surface from transmitter to receiver. The* twt_1 *is the radar-wave two-way travel time of* $reflector_1$*. An example of CMP data with hyperbolic picks (in red) is shown on the right side of the figure. The left y-axis indicates radar wave two-way travel time in ns, the right axis shows an* *approximate depth (m), assuming a constant radar velocity in firn of 0.21 m ns^{-1}, and the top x-axis is the distance in m.*

Figure S2 illustrates the basic processing flowchart for both GPR transect and CMP data, followed by 1-D CMP velocity analysis using Semblance analysis in ReflexW software (Sandmeier, 2010). We applied a sequence of processing steps, such as filters and gain, to remove apparent noise and improve the radargram visibility. To adjust the first arrival at the surface, we used the move start time and applied de-wow along with bandpass Butterworth filters to increase the signal-to-noise ratio. Background removal and static correction steps help to reduce system-induced irregularities (Patil et al 2025). Detailed parameter settings and values for the semblance analysis are given in Table 3 in the main text. The processing steps indicated in the flowchart (Fig. S2) depend on the quality of the acquired data. Some steps may vary depending on the noise level, the GPR system used during the measurement, and the requirement for radargram interpretation. Figure S3 shows screenshots of the interactive adaptation (Fig. S3a) and semblance analysis (Fig. S3b) within CMP 1-D velocity analysis using ReflexW software, with parameter values suitable for the acquired dataset.

The use of the dielectric mixing model helps to derive the physical properties of the subsurface medium from the radar wave propagation velocity (Topp et al., 1980; Endres et al., 2009). Estimating the reflector depth by converting the radar travel time to depth with the help of the radar wave velocity derived from the mixing model (Looyenga, 1965) as

$$\varepsilon_{mix}^{1/3} = (1 - v_1)\,\varepsilon_1^{1/3} + v_2\varepsilon_2^{1/3} \quad \text{..........Eq S1}$$

Here, ε_{mix} is an effective relative permittivity of the mixture and ε_1 and ε_2 are relative permittivities of pure components. Whereas v_1 and v_2 are the volume fractions of components.

The depth of each IRH identified in CMP-gathered data is analysed using the CMP-1D-analysis method as stated in the processing flowchart, Figs S2 and S3, using ReflexW software (Sandmeier, 2010). The hyperbolic reflection picking procedure to derive the radar velocity-depth profile is detailed in Patil et al (2025). Here, we briefly describe the same procedure. For the static time correction, by assuming a wave velocity of 0.3 *m ns*$^{-1}$, the linear-approximated direct wave is shifted to zero offset as in Fig S1b. The semblance analysis was carried out by setting the input parameters in the interactive adaptation and semblance analysis window, as shown in Figs S3a and S3b. The best-fitting root-mean-square velocity (V_{rms}) can be selected from the correlation histogram for visible hyperbolic reflection (Fig. S1b). The same process is continued for the remaining reflection hyperbolas (red lines in Fig. S1b). Thus, corresponding modelled velocities can be obtained from the picked V_{rms} for each hyperbola (Figs S4c, S5c, S6c and S7c). We provide examples of all representative semblance panels for each CMP data set gathered at each location and measured year, as in Figures S4, S5, S6 and S7. The parameter values, such as dv, min and max vel, and delta depth (Figs S3a and b), can vary depending on the user's requirements for visualising the CMP radargram (Figs S5c, S6c and 7c). Figure 2 in the main text represents the semblance panel of the CMP gathered from Ewigschneefeld in 2025. Further details of density inversions from CMP-estimated interval velocity are provided in the main text, method section 4.2.

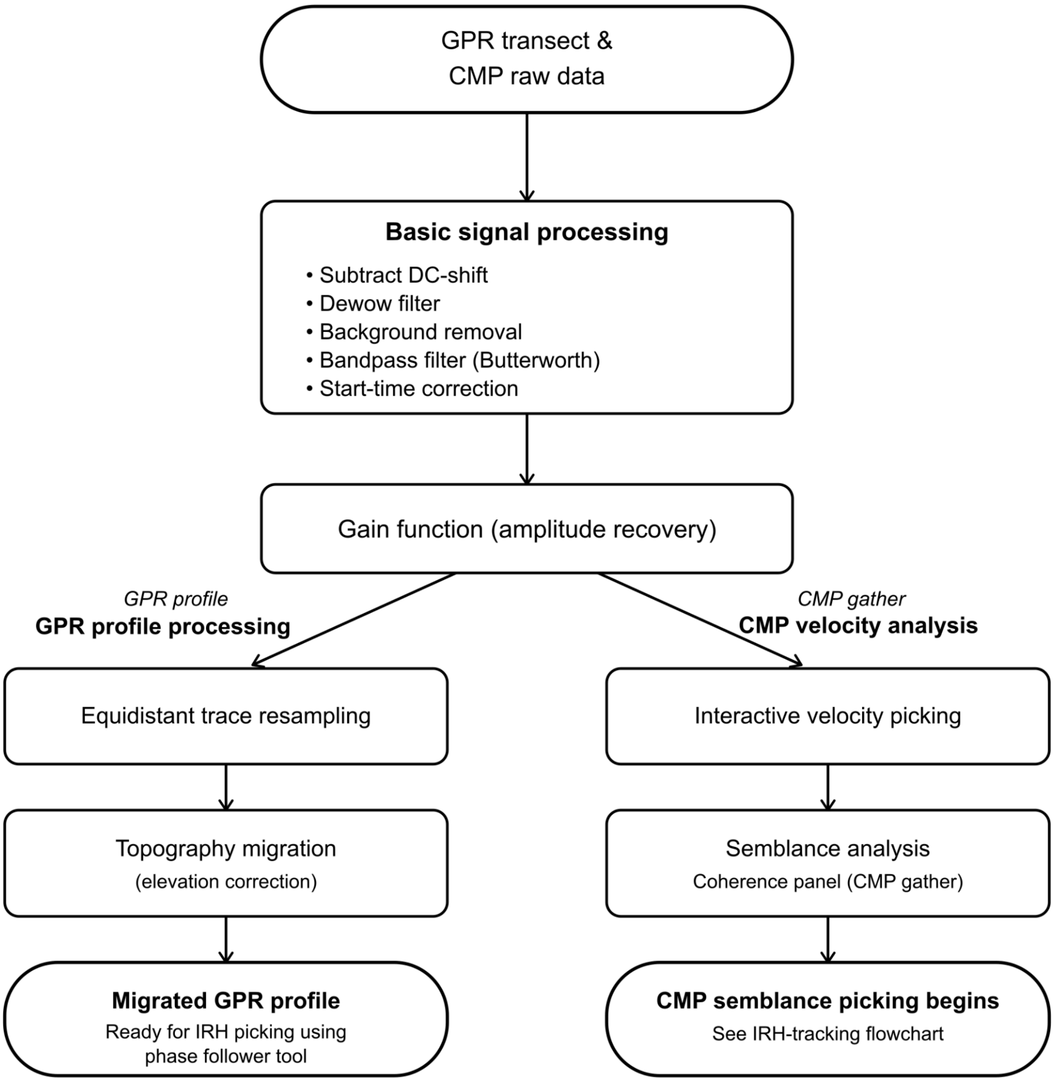

Figure S2: Flowchart demonstrating the CMP gather and GPR transect data processing steps.

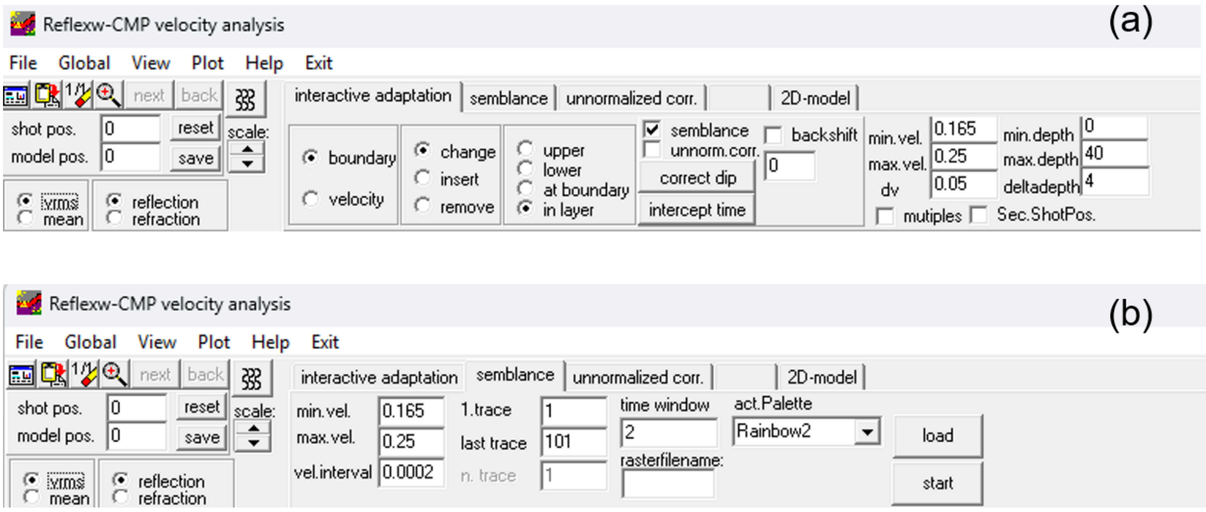

Figure S3. Screenshots of CMP data semblance analysis using a CMP-1D velocity analysis window in ReflexW software (Sandmeier, 2010). *(a) parameter settings within the interactive adaptation window and (b) parameter values for the semblance 1-D model run to get the* V_{rms} *values with depth.*

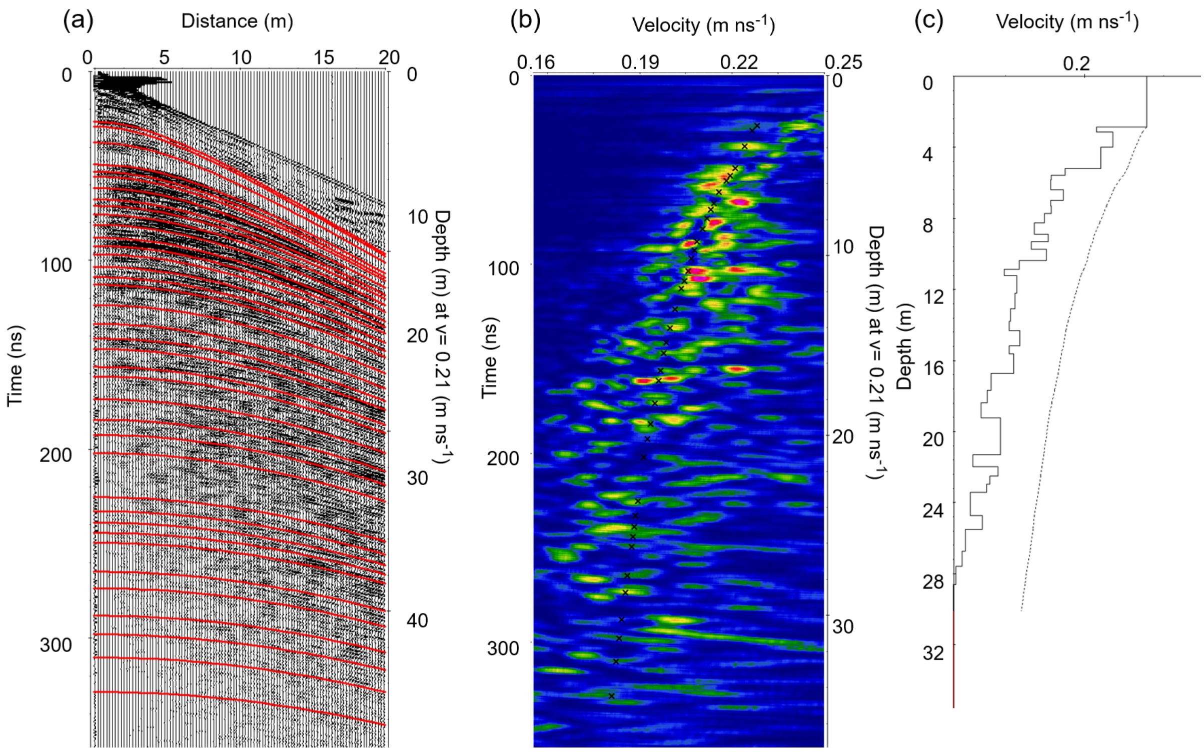

Figure S4: Ewig Down 2025. The semblance analysis of the common mid-point (CMP) data gathered at the Ewigschneefeld (CMP3 in Fig. 1) in 2025. The picked hyperbolic pattern or internal reflection horizons (IRHs) using ReflexW software (a) matches the energy coherence *(b), representing* V_{rms} *velocities corresponding to the semblance pick. The 1-D modelled interval velocity for the picked* V_{rms} *is shown on the right part (c) of the figure. The dotted line shows the picked* V_{rms}*, and the solid line indicates the corresponding interval velocity. The left y-axis in the figures (a and b) represents the radar wave two-way travel time (TWT) in ns. The right y-axis of the figures (a) and (b) indicates an approximate depth (m), assuming a constant radar velocity in firn of 0.21 m* ns^{-1}*. In panel (c), the left y-axis shows the depth adjusted to the modelled interval velocity. The x-axis in panel (a) is the distance in metres, and in panels (b) and (c), the pickable* V_{rms} *velocity for the corresponding semblance energy.*

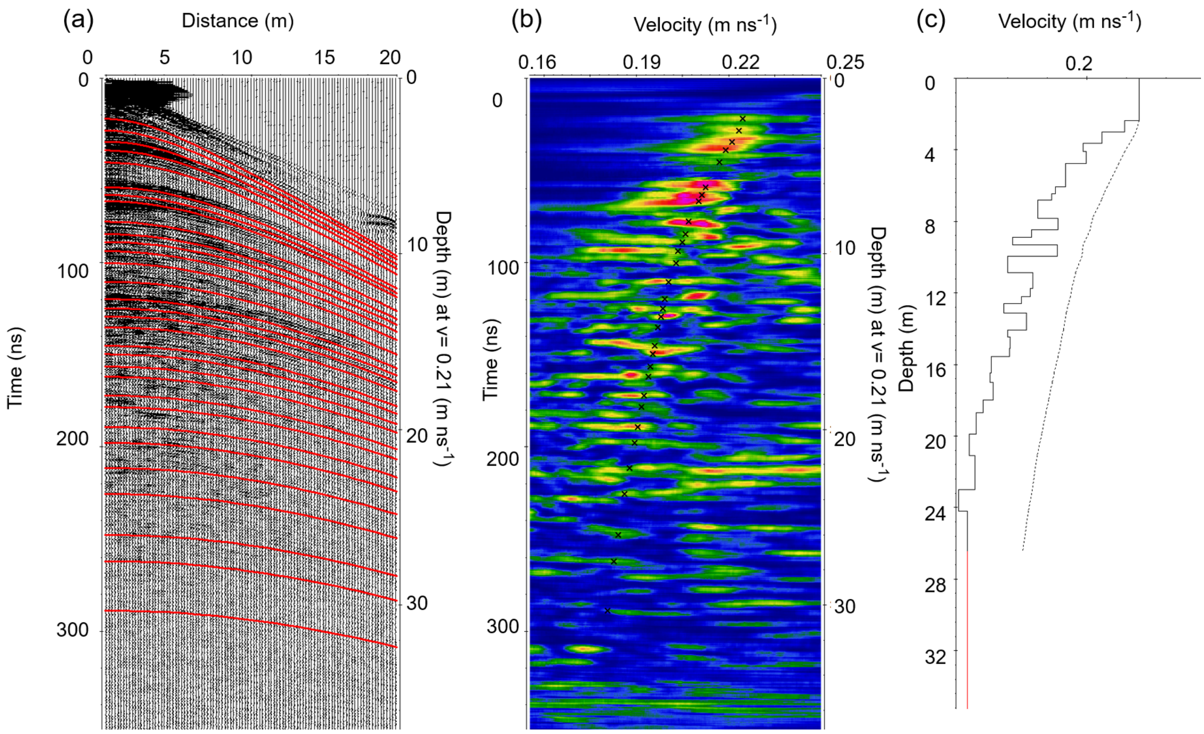

Figure S5: Stake 2025. The semblance analysis of the common mid-point (CMP) data gathered at the Stake near Jungfraufirn (CMP4 in Fig. 1) in 2025. The picked hyperbolic pattern or internal reflection horizons (IRHs) using ReflexW software (a) matches the energy coherence (b), representing V_{rms} *velocities corresponding to the semblance pick. The 1-D modelled interval velocity for the picked* V_{rms} *is shown on the right part (c) of the figure. The dotted line shows the picked* V_{rms}*, and the solid line indicates the corresponding interval velocity. The left y-axis in the figures (a and b) represents the radar wave two-way travel time (TWT) in ns. The right y-axis of the figures (a) and (b) indicates an approximate depth (m), assuming a constant radar velocity in firn of 0.21 m* ns^{-1}*. In panel (c), the left y-axis shows the depth adjusted to the modelled interval velocity. The x-axis in panel (a) is the distance in metres, and in panels (b) and (c), the pickable* V_{rms} *velocity for the corresponding semblance energy.*

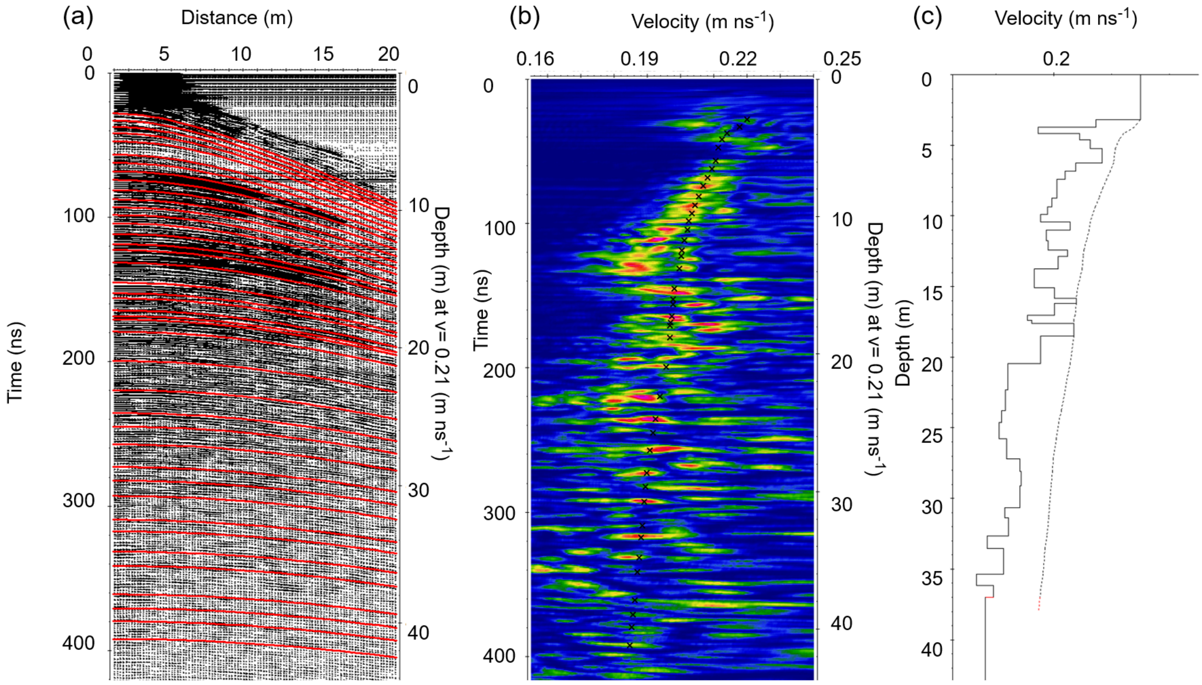

Figure S6: Ewig up 2024. The semblance analysis of the common mid-point (CMP) data gathered at the upper part of the Ewigschneefeld (CMP2 in Fig. 1) in 2024. The picked hyperbolic pattern or internal reflection horizons (IRHs) using ReflexW software (a) matches the energy coherence (b), representing V_{rms} *velocities corresponding to the semblance pick. The 1-D modelled interval velocity for the picked* V_{rms} *is shown on the right part (c) of the figure. The dotted line shows the picked* V_{rms}*, and the solid line indicates the corresponding interval velocity. The left y-axis in the figures (a and b) represents the radar wave two-way travel time (TWT) in ns. The right y-axis of the figures (a) and (b) indicates an approximate depth (m), assuming a constant radar velocity in firn of 0.21 m ns*$^{-1}$*. In panel (c), the left y-axis shows the depth adjusted to the modelled interval velocity. The x-axis in panel (a) is the distance in metres, and in panels (b) and (c), the pickable* V_{rms} *velocity for the corresponding semblance energy.*

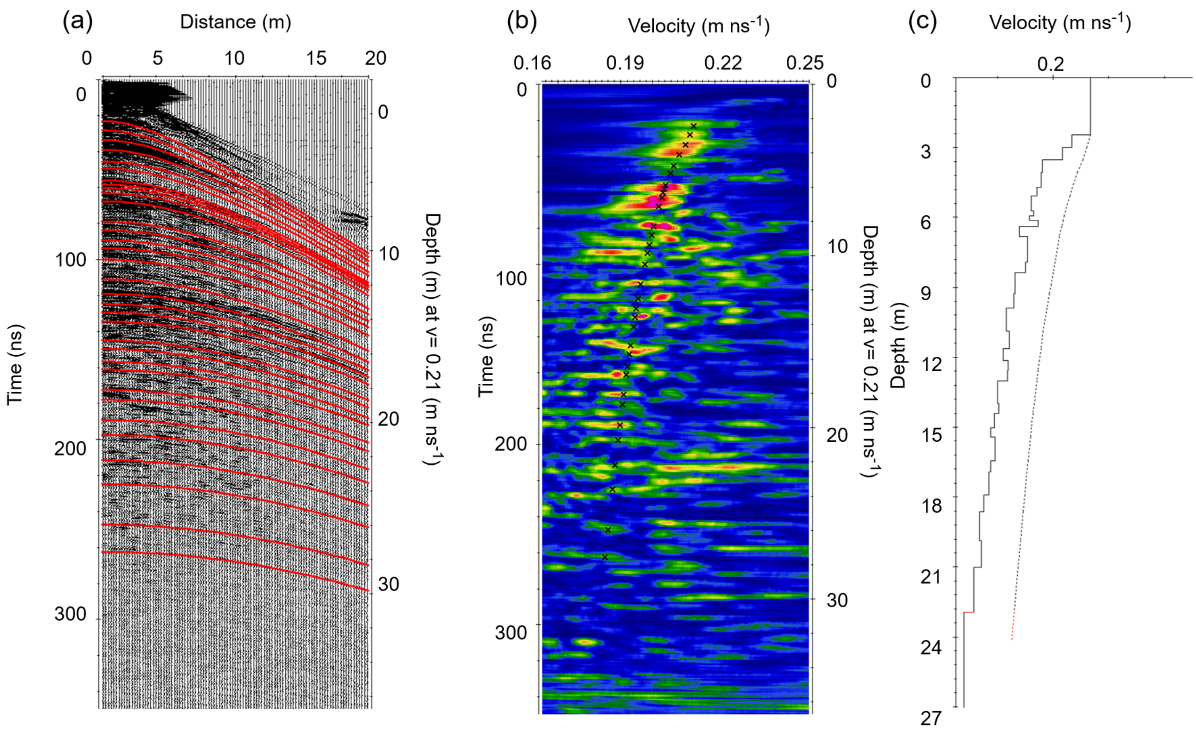

Figure S7: Stake 2024. The semblance analysis of the common mid-point (CMP) data gathered at the Stake near Jungfraufirn (CMP4 in Fig. 1, main text) in 2024. The picked hyperbolic pattern or internal reflection horizons (IRHs) using ReflexW software (a) matches the energy coherence (b), representing V_{rms} *velocities corresponding to the semblance pick. The 1-D modelled interval velocity for the picked* V_{rms} *is shown on the right part (c) of the figure. The dotted line shows the picked* V_{rms}*, and the solid line indicates the corresponding interval velocity. The left y-axis in the figures (a and b) represents the radar wave two-way travel time (TWT) in ns. The right y-axis of the figures (a) and (b) indicates an approximate depth (m), assuming a constant radar velocity in firn of 0.21 m* ns^{-1}*. In panel (c), the left y-axis shows the depth adjusted to the modelled interval velocity. The x-axis in panel (a) is the distance in metres, and in panels (b) and (c), the pickable* V_{rms} *velocity for the corresponding semblance energy.*

S1.2 IRH tracking procedure

IRH tracing for the long GPR transect (Fig. 1 main text) can be performed using a semi-automatic phase follower tool in ReflexW, as shown in Figure 3 main text. Picking IRHs from CMP data, as already explained in this supplement. The process of identifying picked CMP-derived IRHs as annual layers by comparing them with the stake-measured point mass balance is described in our previous study, Patil et al. (2025). The flow chart of the same is provided in Figure S8. The results to validate the matching of CMP-based SWE with the stake-measured SWE are given in the main text appendix Figure A2.

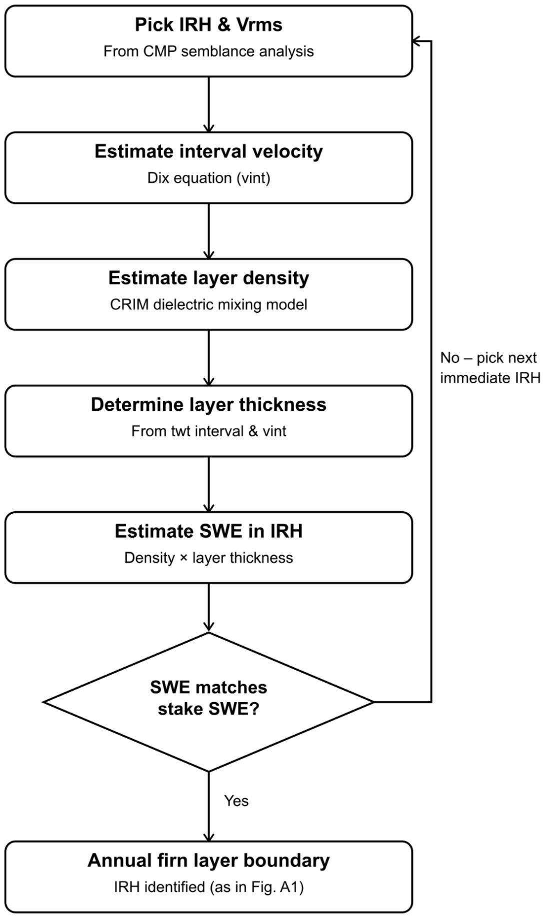

Figure S8: Flow chart illustrating an iterative process of identifying CMP IRHs as annual layers as explained in Patil et al (2025).

S1.3 Firn core analysis

Acquired firn core samples from FC3 (Fig. 1 in the main text) were analysed in the laboratory of the Geozentrum Nordbayern at Friedrich-Alexander Universität Erlangen-Nürnberg for stable isotopes and chemical impurities. Oxygen and hydrogen stable water isotopes ($\delta^{18}O$ and $\delta^{2}H$) were analysed using laser spectroscopy. Water samples were analysed using an isotope ratio infrared spectroscopy (IRIS) analyser, which employs wavelength-scanned cavity ring-down spectroscopy. All values reported after the laboratory analysis are in the standard δ-notation measured in per min (‰) vs Vienna Standard Mean Ocean Water (VSMOW) as per

$\delta = (R_{sample} / R_{reference} - 1)$ ……………… Eq S2

Here, R is the ratio of heavy to light isotope numbers of a measured sampled element (Coplen, 2011).

Each sample was measured four times by injecting in a sequential order, and the raw data were corrected for sample-to-sample memory to estimate the mean values. Data sets were corrected for instrumental drift during the run and normalised to the VSMOW/SLAP (Standard Light Antarctic Precipitation) scale by assigning a value of 0 ‰ and –55.5 ‰ (18O) / 0 ‰ and -427.5 ‰ (2H) to VSMOW2 and SLAP2 by following Brand et al. (2004). Further detailed description of the procedure can be found in van Geldern and Barth (2012). Whereas major ions such as Na, Ca, Fe and Ti were analysed on an iCAP Qc inductively coupled plasma - mass spectrometer (ICP-MS) (Thermo Fisher Scientific Inc., Bremen, Germany) fed by a SC-2DXS autosampler (Elemental Scientifics, Omaha, NV, U.S.A). The process includes measuring the sample three times and then stabilising it with two drops of 65% HNO_3.

S1.4 Strain contribution to IRH thinning

To quantify the effect of vertical strain rate on the estimated compaction rate (Fig. 11a in main text), we need vertical velocity, estimated as

$\epsilon_{zz} = -(\epsilon_{xx} + \epsilon_{yy})$.......EqS3 (Cuffey and Paterson, 2010)

Here, ϵ_{xx} and ϵ_{yy} are horizontal strain rates in the x and y directions, respectively. Assuming ϵ_{xx} and ϵ_{yy} based on available Millan et al (2022) and Leinss and Bernhard (2021) ice velocity data, the vertical strain over the 13.4 m-thick firn pack (commonly identified as the last annual layer 2015 from referencing the 2023 layer) is estimated as

$\dot{\epsilon}_{zz} = \epsilon_{zz} X H$ EqS4
Here, H is the thickness between 2023-2015 firn layers

The worked example is as here, assuming a vertical strain of 0.02 a^{-1} . Considering the velocity gradient of 20 $m\,a^{-1}$ over 1000 m, the resulting vertical strain over a 13.4 m thick firn pack would be 0.264 $m\,a^{-1}$.
Considering the estimated vertical strain rate of 0.264 $m\,a^{-1}$, the contribution to the firn pack displacement is 22.33 % for the estimated compaction of the firn pack of 1.2 $m\,a^{-1}$. This implies the vertical strain contribution is around 22% of the estimated compaction rate.

S2 Specific notes related to the Result section

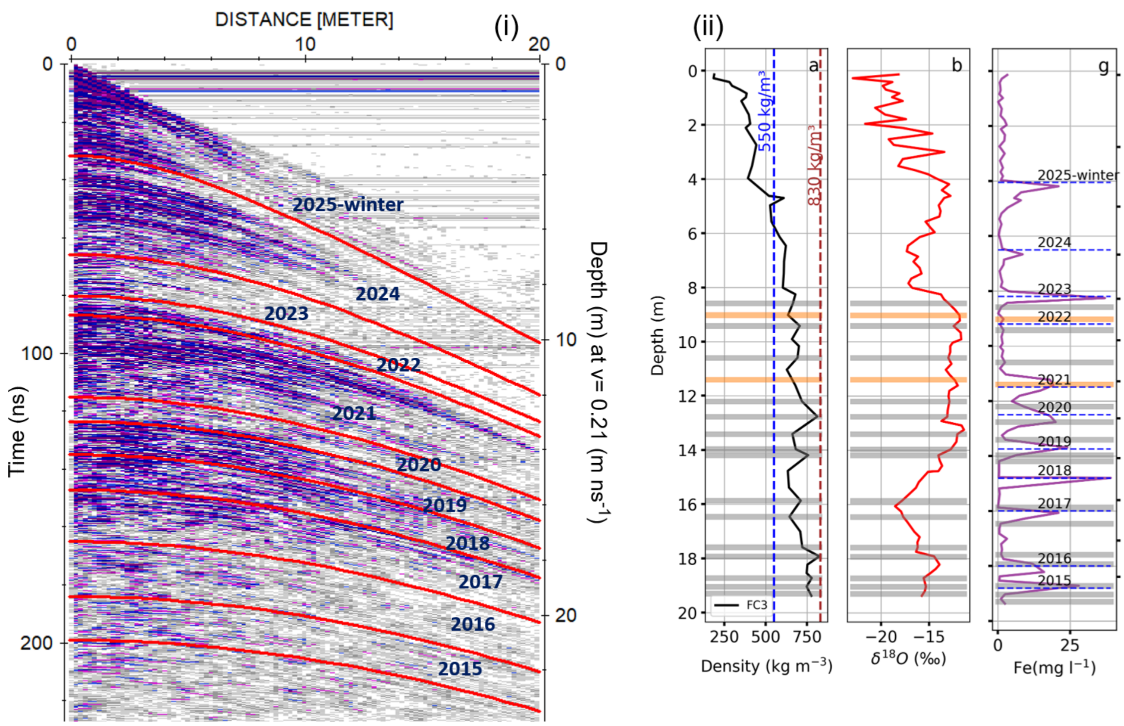

Figure S9: Illustration of annotated identified IRHs as annual layers (red lines in (i)) from the CMP gathered at the upper part of Ewigschneefeld (CMP2 in Fig. 1 main text) in 2025 (i). It should be considered that the annotated IRH's depth (m) on the right y-axis (i) is approximated by assuming a constant radar velocity in firn of 0.21 m ns^{-1}*. The left y-axis (i) is the radar wave two-way travel time in (ns). Matched annual layers derived from FC3 along with firn density-depth profile, oxygen isotope, and one of the major ions, Fe (ii), as shown in Fig 5, main text.*

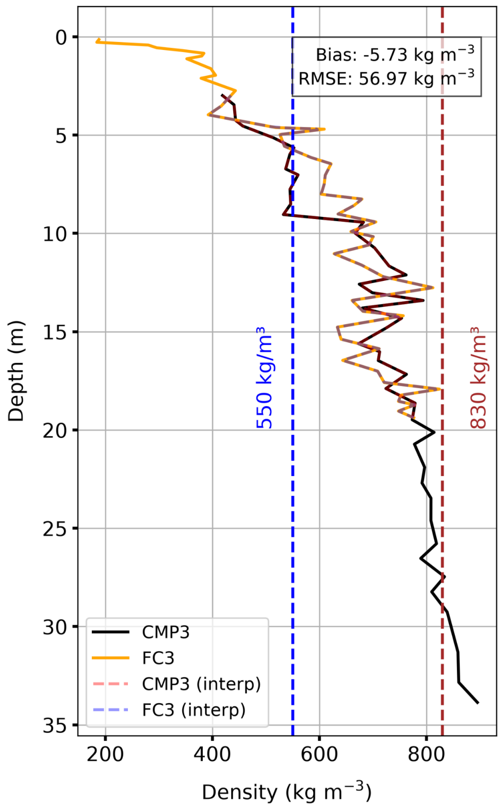

Figure S10: Comparison of firn core (FC3) and CMP-derived (CMP3) density-depth profiles along with the estimated bias and RMSE up to a common depth.

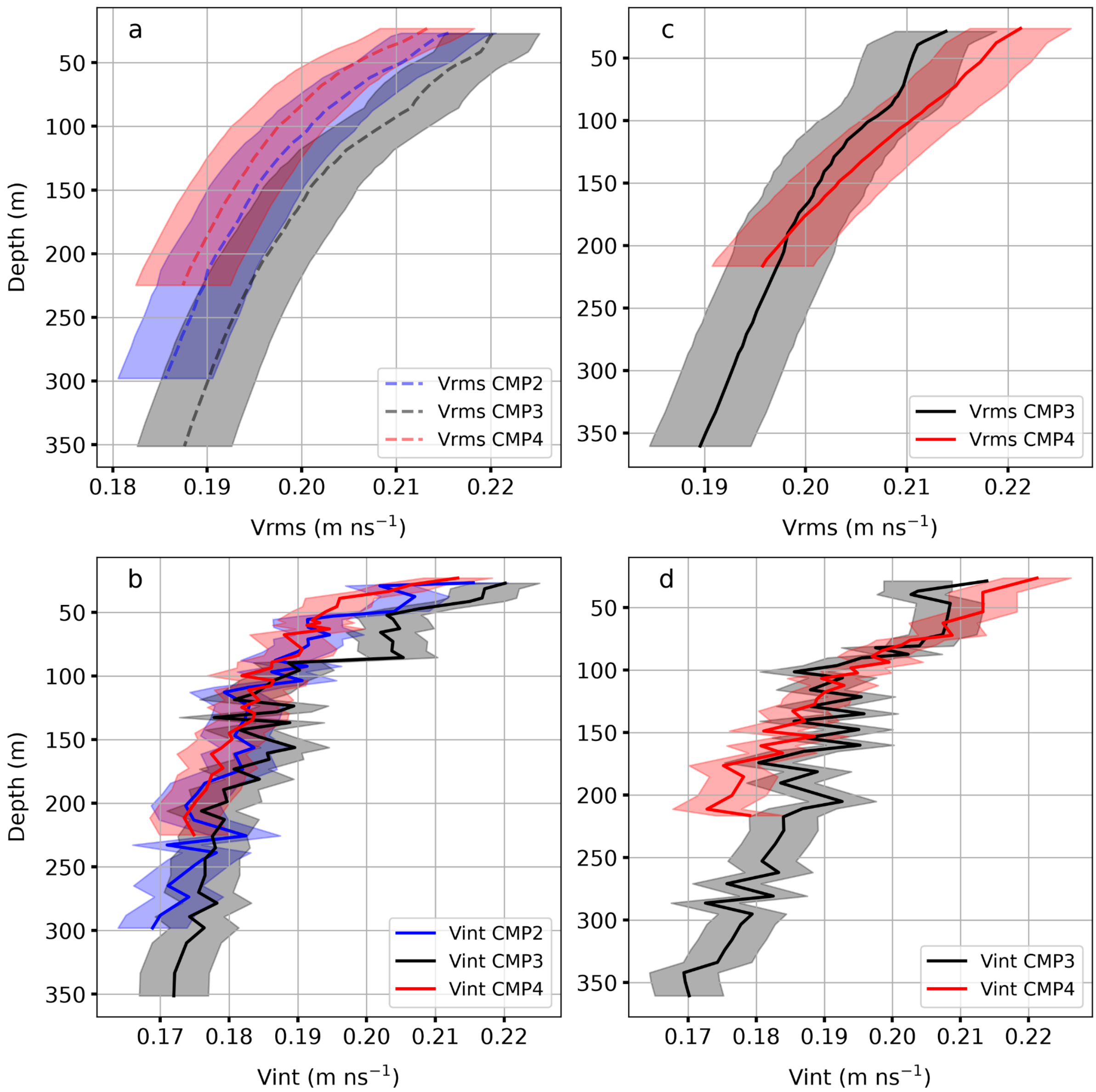

Figure S11: Illustration of semblance-picked V_{rms} at three locations from CMP gathered during the 2025 (a) and corresponding estimated interval velocities (Vint) with error bars for the 0.005 m ns^{-1} uncertainty in picking as suggested by Patil et al (2025) and Booth et al (2011). Similar V_{rms} semblance picks used in this research were gathered at two CMP locations during the 2024 campaign (c), as in Fig 1 in the main text and corresponding estimated interval velocities with uncertainty (d).

2.1 CMP data quality

The following Figures S12, S13, S14, and S15 demonstrate the quality of CMP data after processing, acquired in the upper part of Ewigschneefeld during the 2024 and 2025 campaigns. All remaining data will be provided upon the acceptance of the manuscript as stated in the data availability section.

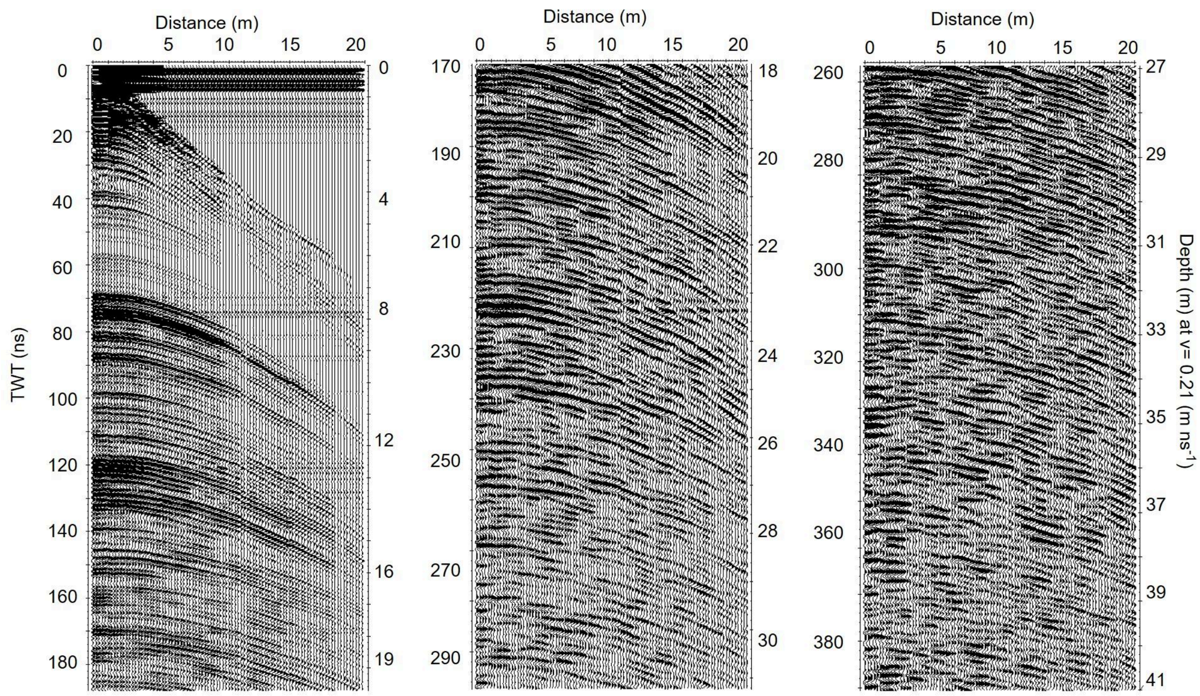

Figure S12: Illustration of the processed CMP3 2024 gather reveals clear internal reflection horizons (IRHs), including deeper features beyond 250 ns (~25 m). The x-axis represents the horizontal position of the CMP acquisition, while the left y-axis shows the radar two-way travel time in nanoseconds. The right y-axis converts this travel time to depth using an assumed firn radar velocity of 0.21 m ns^{-1} (Patil et al, 2025).

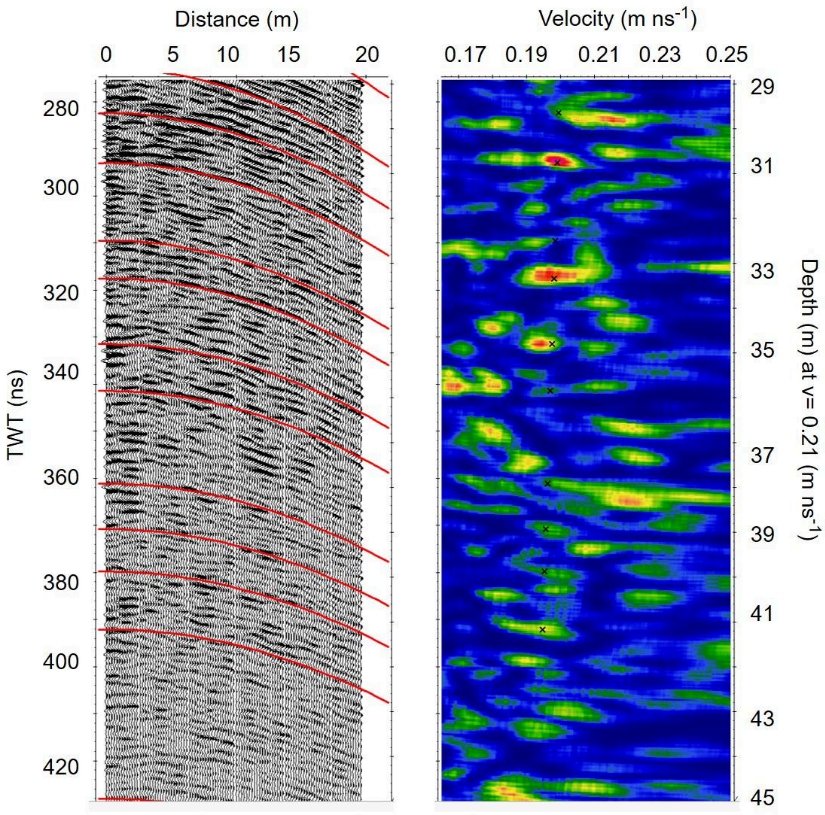

Figure S13: Illustration of the pickable V_{rms} *velocity from the semblance analysis of the CMP3 data allows reliable picking of Vrms velocities associated with the deeper hyperbolic reflections shown in Fig. A1. Hyperbolas remain identifiable down to 400 ns, and the corresponding Vrms values can be extracted from the semblance panel (right figure). As in the CMP gather, the left y-axis displays radar two-way travel time, while the right y-axis shows depth calculated using a firn velocity of 0.21 m ns*$^{-1}$*. The x-axis indicates horizontal distance (left) and the Vrms velocity in m ns*$^{-1}$ *(right) (Patil et al, 2025).*

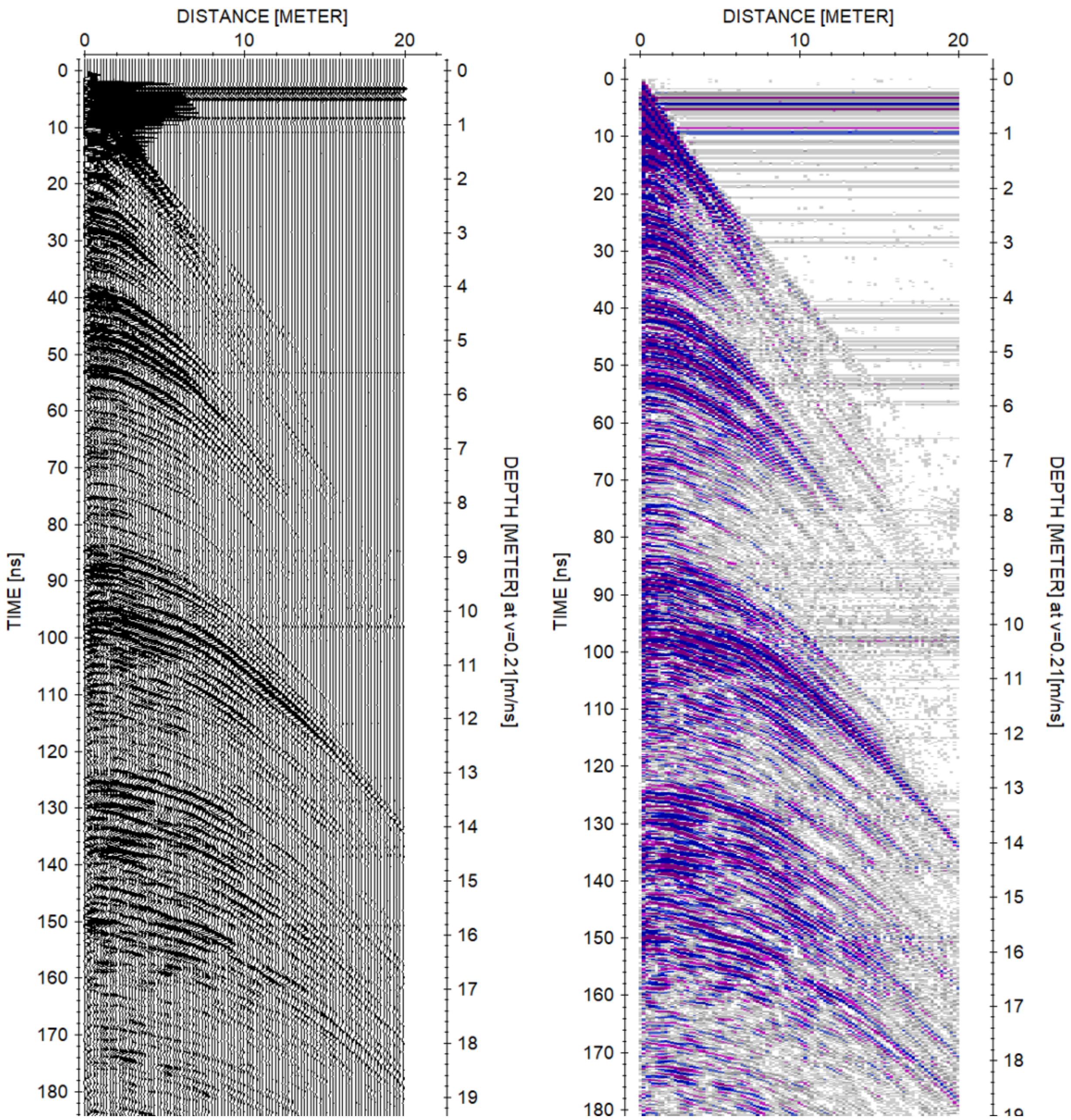

Figure S14: Illustration of the processed CMP3 2025 gather reveals clear internal reflection horizons (IRHs). The x-axis represents the horizontal position of the CMP acquisition, while the left y-axis shows the radar two-way travel time in nanoseconds. The right y-axis converts this travel time to depth, assuming a firn radar velocity of 0.21 m ns^{-1}.

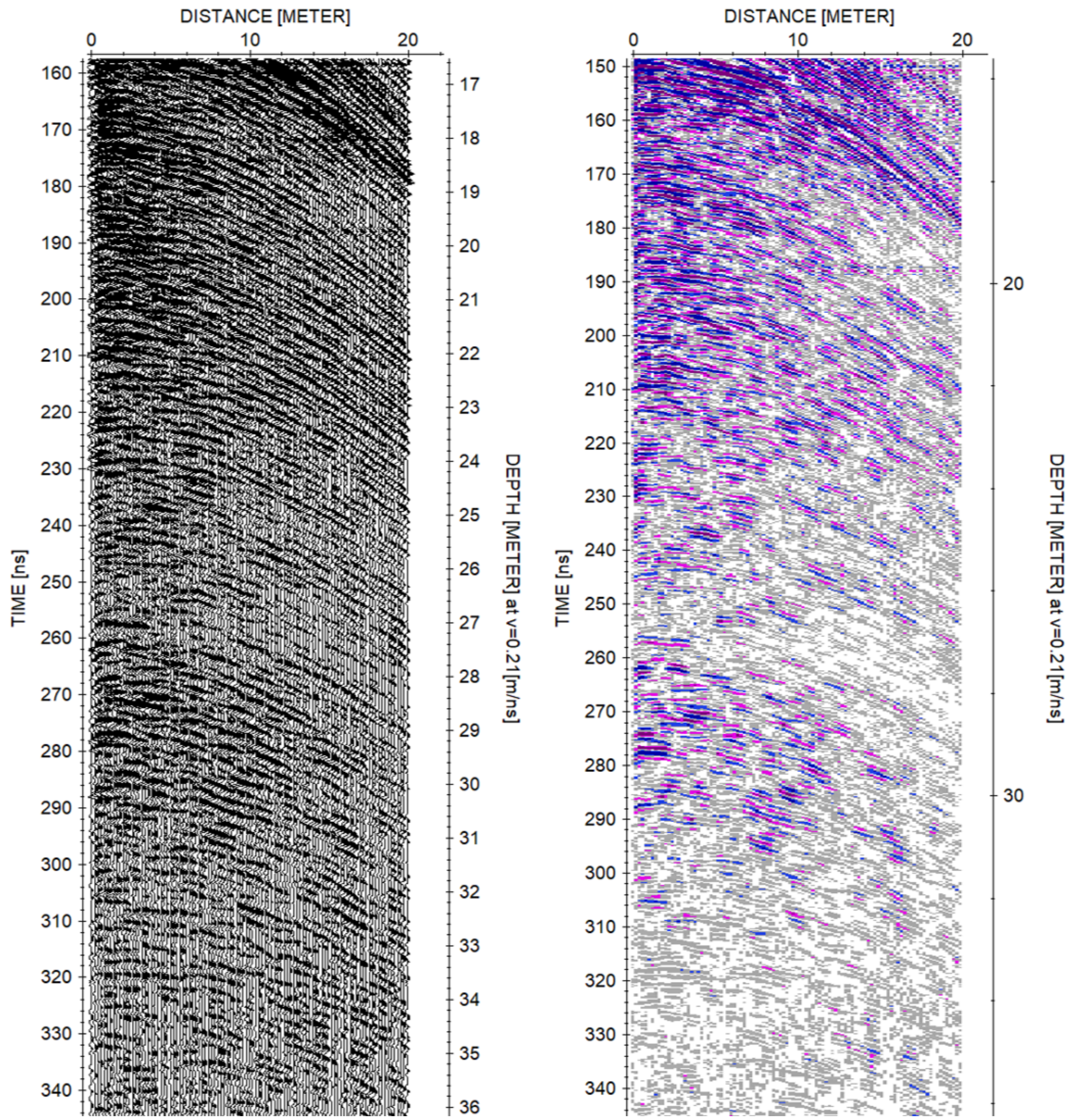

Figure S15: Illustration of the processed CMP3 2025 gather reveals clear internal reflection horizons (IRHs), including deeper features beyond 250 ns (~25 m). The x-axis represents the horizontal position of the CMP acquisition, while the left y-axis shows the radar two-way travel time in nanoseconds. The right y-axis converts this travel time to depth, assuming a firn radar velocity of 0.21 m ns^{-1}.

References

Booth, A. D., Clark, R. A., and Murray, T.: Influences on the resolution of GPR velocity analyses and a Monte Carlo simulation for establishing velocity precision, Near Surface Geophysics, 9, 399–411, https://doi.org/10.3997/1873-0604.2011019, 2011.

Cuffey, K. M. and Paterson, W. S. B.: The Physics of Glaciers, Butterworth-Heinemann, Oxford, 4 edn., ISBN 978-0-12-369461-4, https://booksite.elsevier.com/samplechapters/9780123694614/01~Front_Matter.pdf, last accessed: 21 October 2025, 2010.

Coplen, T. B.. Guidelines and recommended terms for expression of stable-isotope-ratio and gas-ratio measurement results. - Rapid Communications in Mass Spectrometry, 25, 2538-2560, https://doi:10.1002/rcm.5129, 2011

Leinss, S. and Bernhard, P.: TanDEM-X: Deriving InSAR Height Changes and Velocity Dynamics of Great Aletsch Glacier, IEEE Journal of Selected Topics in Applied Earth Observations and Remote Sensing, 14, 4798–4815, https://doi.org/10.1109/JSTARS.2021.3078084, 2021.

Millan, R., Mouginot, J., Rabatel, A., et al.: Ice velocity and thickness of the world's glaciers, Nature Geoscience, 15, 124–129, https://doi.org/10.1038/s41561-021-00885-z, 2022.

Patil, A. M., Mayer, C., Seehaus, T., Groos, A. R., and Bauder, A.: Investigating firn structure and density in the accumulation area of the Grosser Aletschgletscher using ground-penetrating radar, The Cryosphere, 19, 5547–5577, https://doi.org/10.5194/tc-19-5547-2025, 2025b.

van Geldern, R. and Barth, J.A.C.: Optimisation of instrument setup and post-run corrections for oxygen and hydrogen stable isotope measurements of water by isotope ratio infrared spectroscopy (IRIS). - Limnology and Oceanography: Methods, 10, 1024-1036, https://doi.org/10.4319/lom.2012.10.1024, 2012